New calculation for ^{2}H($e, e'p$)n at GeV energies

Sabine Jeschonnek[1] and J. W. Van Orden[2,3]
[1]*Ohio State University, Physics Department, Lima, Ohio 45804, USA*
[2]*Department of Physics, Old Dominion University, Norfolk, Virginia 23529, USA*
[3]*Thomas Jefferson National Accelerator Facility, 12000 Jefferson Ave., Newport News, Virginia 23606, USA*
(Received 21 May 2008; published 29 July 2008)

We perform a fully relativistic calculation of the ^{2}H($e, e'p$)n reaction in the impulse approximation. We employ the Gross equation to describe the deuteron ground state, and we use the SAID parametrization of the full NN scattering amplitude to describe the final state interactions (FSIs). We include both on-shell and positive-energy off-shell contributions in our FSI calculation. We show results for momentum distributions and angular distributions of the differential cross section, as well as for various asymmetries. We identify kinematic regions where various parts of the FSIs are relevant, and discuss the theoretical uncertainties connected with calculations at high missing momenta.

DOI: 10.1103/PhysRevC.78.014007 PACS number(s): 25.30.Fj, 21.45.Bc, 24.10.Jv

I. INTRODUCTION

Exclusive electron scattering from the deuteron target is not only very interesting by itself but also a very relevant stepping stone toward understanding exclusive electron scattering from heavier nuclei. The ^{2}H($e, e'p$)n reaction at GeV energies allows us—and requires us—to carefully study the reaction mechanism. It is necessary to consider final state interactions (FSIs) between the two nucleons in the final state, two-body currents, and isobar contributions. Of these, the FSIs can be expected to be the most relevant part of the reaction mechanisms at the GeV energy and momentum transfers relevant to the study of the transition from hadronic to quark-gluon degrees of freedom. For some recent reviews on this exciting topic, see, e.g., Refs. [1–3].

Even though the deuteron is the simplest nucleus and has been the subject of considerable attention for a long time, there are several open questions: Is it possible to experimentally determine the high-momentum components of the deuteron wave function even though the nuclear wave function or the momentum distribution are not observables? Will conventional nuclear physics break down or become too cumbersome at some point, and will a description involving quarks become necessary? Are there any six-quark admixtures in the deuteron wave function, and do they have an unambiguous experimental signal? What influence does short-range physics have on conventional wave functions, and how can this influence be removed to find an effective potential $V_{\mathrm{low}k}$, provided one is interested only in low-energy scenarios [4,5]? Relativistic wave functions are available [6] for the deuteron. And while the calculational effort is still considerable, it can be managed without resorting to super computers. The interest and importance of the ^{2}H($e, e'p$)n process is reflected in the fact that a deuteron benchmarking project has been started recently to investigate the differences between various calculations that are based on nonrelativistic wave functions [7].

Anything that we learn about the reaction mechanism of the ^{2}H($e, e'p$)n reaction has implications for heavier targets and for experiments that use the deuteron as a laboratory. Some examples of the latter are the measurement of the neutron magnetic form factor by measuring a ratio of ^{2}H($e, e'p$) and ^{2}H($e, e'n$) cross sections. This allows a significant reduction in the model dependence of the extracted form factor, but some theoretical input is still required [8]. Another example of using the nucleus as a laboratory is color transparency. While meson production from nuclei [9–12] is the main thrust of color transparency investigations, color transparency in ($e, e'p$) reactions is very interesting and topical, too [13]. To study color transparency, one first needs to establish a firm understanding of all the conventional nuclear effects.

Several experiments on deuteron targets have been performed in the last few years, at both Jefferson Lab and MIT Bates, and these data either have been published recently or are currently under analysis [8,14–17]. There are also new proposals for ^{2}H($e, e'p$) experiments at Jefferson Lab [18]. Apart from these exciting new data, there are very interesting open questions posed by data that have been available for some years now [19–22]. Regardless of the momentum transfers involved, there has been a discrepancy between data and calculations at low missing momentum. We discuss calculations in kinematics relevant to the new experiments as well as the low missing momentum puzzle in our results section.

The experimental activity in ($e, e'p$) reactions on the deuteron and other light nuclei has been matched by theoretical efforts. These calculations typically are performed using Glauber theory, the generalized eikonal approximation [23–25], or a diagrammatic approach [26], although there are rare exceptions [27]. Even a second-order correction to the eikonal approximation has been suggested recently [28]. Many of these calculations focus only on the differential cross section and use just the central part of the NN scattering amplitude. Currently, almost all calculations for ^{2}H($e, e'p$)n reactions are unfactorized [29], but factorized approaches are used for heavier targets [30]. A common feature first introduced in Glauber calculations is the assumption that the momentum transfer in the rescattering of the two nucleons is purely transverse. This has consequences for both the profile function

and the argument for which the NN scattering amplitude is evaluated.

In this paper, we present a new calculation with several important features: We use a fully relativistic formalism and describe the ground state with a solution of the Gross equation [31]; we include all parts of the nucleon-nucleon scattering amplitude, including all the spin-dependent parts, and use a realistic, modern parametrization; the only approximation that we make is to neglect the negative energy states, as discussed at the end of the first section. This new calculation can be used at all energy and momentum transfers, provided that an appropriate full set of pn scattering data is available. This paper is organized as follows: First, we review the theoretical framework for our calculations, then we show numerical results for the cross section and asymmetries. We conclude with a summary and outlook.

II. THEORETICAL FRAMEWORK

The Feynman diagrams representing the impulse approximation are shown in Fig. 1. Figure 1(a) represents the plane wave contribution, and Fig. 1(b) represents the contribution from final state interactions. The plane wave contribution to the current matrix element is given by

$$\langle \boldsymbol{p}_1 s_1; \boldsymbol{p}_2 s_2 | J^{\mu}_{\mathrm{PW}} | \boldsymbol{P} \lambda_d \rangle = -\bar{u}(\boldsymbol{p}_1, s_1)\Gamma^{\mu}(q) G_0(P - p_2)\Gamma^{T}_{\lambda_d}(p_2, P)\bar{u}^{T}(\boldsymbol{p}_2, s_2), \quad (1)$$

where the target deuteron has four-momentum P and spin λ_d, the final proton has four-momentum p_1 and spin s_1, and the final neutron has four-momentum p_2 and spin s_2. The single-nucleon propagator is

$$G_0(p) = \frac{\gamma \cdot p + m}{m^2 - p^2 - i\eta}, \quad (2)$$

and the current operator is chosen to be of the free Dirac-plus-Pauli form

$$\Gamma^{\mu}(q) = F_1(Q^2)\gamma^{\mu} + \frac{F_2(Q^2)}{2m} i\sigma^{\mu\nu} q_{\nu}. \quad (3)$$

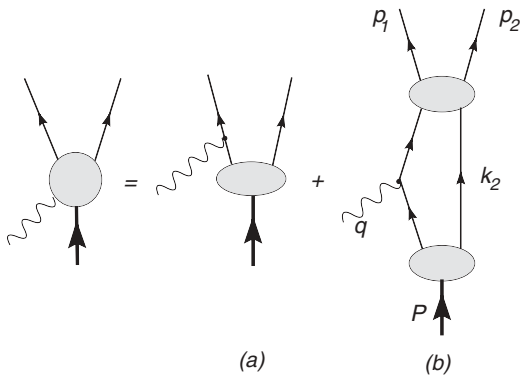

FIG. 1. Feynman diagrams representing the impulse approximation.

The deuteron vertex function with nucleon 2 on-shell can be written as

$$\Gamma_{\lambda_d}(p_2, P) = g_1\big(p_2^2, p_2 \cdot P\big)\gamma \cdot \xi_{\lambda_d}(P) + g_2\big(p_2^2, p_2 \cdot P\big) \times \frac{p \cdot \xi_{\lambda_d}(P)}{m} - \Big(g_3\big(p_2^2, p_2 \cdot P\big)\gamma \cdot \xi_{\lambda_d}(P) + g_4\big(p_2^2, p_2 \cdot P\big)\frac{p \cdot \xi_{\lambda_d}(P)}{m}\Big)\frac{\gamma \cdot p_1 + m}{m} C, \quad (4)$$

where $p_1 = P - p_2$, $p = \frac{1}{2}(p_1 - p_2) = \frac{P}{2} - p_2$, C is the charge-conjugation matrix, and ξ_{λ_d} is the deuteron polarization four-vector. The invariant functions g_i are given by

$$g_1\big(p_2^2, p_2 \cdot P\big) = \frac{2E_k - M_d}{\sqrt{8\pi}}\left[u(k) - \frac{1}{\sqrt{2}}w(k) + \sqrt{\frac{3}{2}}\frac{m}{k}v_t(k)\right], \quad (5)$$

$$g_2\big(p_2^2, p_2 \cdot P\big) = \frac{2E_k - M_d}{\sqrt{8\pi}}\left[\frac{m}{E_k + m}u(k) + \frac{m(2E_k + m)}{\sqrt{2}k^2}w(k) + \sqrt{\frac{3}{2}}\frac{m}{k}v_t(k)\right], \quad (6)$$

$$g_3\big(p_2^2, p_2 \cdot P\big) = \sqrt{\frac{3}{16\pi}}\frac{mE_k}{k}v_t(k), \quad (7)$$

$$g_4\big(p_2^2, p_2 \cdot P\big) = -\frac{m^2}{\sqrt{8\pi}M_d}\left[(2E_k - M_d)\left(\frac{1}{E_k + m}u(k) - \frac{E_k + 2m}{\sqrt{2}k^2}w(k)\right) + \frac{\sqrt{3}M_d}{k}v_s(k)\right], \quad (8)$$

where

$$k = \sqrt{\frac{(P \cdot p_2)^2}{P^2} - p_2^2} \quad (9)$$

is the magnitude of the neutron three-momentum in the deuteron rest frame, and

$$E_k = \sqrt{k^2 + m^2}. \quad (10)$$

The functions $u(k)$, $w(k)$, $v_s(k)$, and $v_t(k)$ are the s-wave, d-wave, singlet p-wave, and triple p-wave radial wave functions of the deuteron in momentum space. The radial wave functions are normalized in the absence of energy-dependent kernels such that

$$\int_0^{\infty} \frac{dp\, p^2}{(2\pi)^3}\big[u^2(p) + w^2(p) + v_t^2(p) + v_s^2(p)\big] = 1. \quad (11)$$

For convenience, the spectator deuteron wave function can be defined as

$$\psi_{\lambda_d, s_2}(p_2, P) = G_0(P - p_2)\Gamma^{T}_{\lambda_d}(p_2, P)\bar{u}^{T}(\boldsymbol{p}_2, s_2). \quad (12)$$

We choose to normalize this wave function such that in the deuteron rest frame

$$\sum_{s_2} \int \frac{d^3p_2}{(2\pi)^3} \frac{m}{E_{p_2}} \bar{\psi}_{\lambda_d,s_2}(p_2, P)\gamma^0 \psi_{\lambda_d,s_2}(p_2, P) = 1, \quad (13)$$

which is correct only in the absence of energy-dependent kernels [31–33]. The plane wave contribution to the current matrix element can then be written as

$$\langle \boldsymbol{p}_1 s_1; \boldsymbol{p}_2 s_2 | J^\mu_{\rm PW} | \boldsymbol{P} \lambda_d \rangle = -\bar{u}(\boldsymbol{p}_1, s_1)\Gamma^\mu(q)\psi_{\lambda_d,s_2}(p_2, P). \quad (14)$$

The contribution from final state interactions represented by Fig. 1(b) requires an integration for the loop four-momentum k_2 which involves both the deuteron vertex function and the pn scattering amplitude. An equivalent approach is to formulate the problem in terms of the Spectator or Gross equations [31] where the equations for the scattering amplitude and vertex function are rewritten such that one particle is always taken to be on-mass-shell. This approach is manifestly covariant and has been successfully applied to elastic electron scattering from the deuteron [32]. Using this approach, the contribution of the FSI to the current matrix element is given by

$$\begin{aligned}
&\langle \boldsymbol{p}_1 s_1; \boldsymbol{p}_2 s_2 | J^\mu_{\rm FSI} | \boldsymbol{P} \lambda_d \rangle \\
&= \int \frac{d^3k_2}{(2\pi)^3} \frac{m}{E_{k_2}} \bar{u}_a(\boldsymbol{p}_1, s_1)\bar{u}_b(\boldsymbol{p}_2, s_2) M_{ab;cd}(p_1, p_2; k_2) \\
&\quad \times G_{0ce}(P + q - k_2)\Gamma^\mu_{ef}(q) G_{0fg}(P - k_2) \\
&\quad \times \Lambda^+_{dh}(\boldsymbol{k}_2)\Gamma^T_{\lambda_d gh}(k_2, P), \quad (15)
\end{aligned}$$

where M is the pn scattering amplitude,

$$\Lambda^+(\boldsymbol{p}) = \sum_s u(\boldsymbol{p}, s)\bar{u}(\boldsymbol{p}, s) = \frac{\gamma \cdot p + m}{2m} \quad (16)$$

is the positive-energy projection operator, and the Dirac indices for the various components are shown explicitly. Since the single-nucleon propagator can be decomposed as

$$\begin{aligned}
G_0(p) &= -\frac{m}{E_p} \sum_s \left[\frac{u(\boldsymbol{p}, s)\bar{u}(\boldsymbol{p}, s)}{p^0 - E_p + i\epsilon} + \frac{v(-\boldsymbol{p}, s)\bar{v}(-\boldsymbol{p}, s)}{p^0 + E_p - i\epsilon} \right] \\
&= -\frac{m}{E_p} \left[\frac{\Lambda^+(\boldsymbol{p})}{p^0 - E_p + i\epsilon} - \frac{\Lambda^-(-\boldsymbol{p})}{p^0 + E_p - i\epsilon} \right], \quad (17)
\end{aligned}$$

and

$$\frac{1}{p^0 - E_p + i\epsilon} = -i\pi\delta(p^0 - E_p) + \frac{\mathcal{P}}{p^0 - E_p}, \quad (18)$$

Eq. (15) can be written as

$$\begin{aligned}
&\langle \boldsymbol{p}_1 s_1; \boldsymbol{p}_2 s_2 | J^\mu_{\rm FSI} | \boldsymbol{P} \lambda_d \rangle \\
&= \langle \boldsymbol{p}_1 s_1; \boldsymbol{p}_2 s_2 | J^\mu_a | \boldsymbol{P} \lambda_d \rangle + \langle \boldsymbol{p}_1 s_1; \boldsymbol{p}_2 s_2 | J^\mu_b | \boldsymbol{P} \lambda_d \rangle \\
&\quad + \langle \boldsymbol{p}_1 s_1; \boldsymbol{p}_2 s_2 | J^\mu_c | \boldsymbol{P} \lambda_d \rangle, \quad (19)
\end{aligned}$$

where

$$\begin{aligned}
&\langle \boldsymbol{p}_1 s_1; \boldsymbol{p}_2 s_2 | J^\mu_a | \boldsymbol{P} \lambda_d \rangle \\
&= i\pi \sum_{\sigma_2} \int \frac{d^3k_2}{(2\pi)^3} \frac{m}{E_{k_2}} \frac{m}{E_{P+q-k_2}} \\
&\quad \times \delta(P^0 + \nu - E_{k_2} - E_{P+q-k_2}) \bar{u}_a(\boldsymbol{p}_1, s_1)\bar{u}_b(\boldsymbol{p}_2, s_2) \\
&\quad \times M_{ab;cd}(p_1, p_2; k_2) u_d(\boldsymbol{k}_2, \sigma_2)(\Lambda^+(\boldsymbol{P} + \boldsymbol{q} - \boldsymbol{k}_2) \\
&\quad \times \Gamma^\mu(q)\psi_{\lambda_d,\sigma_2}(k_2, P))_c, \quad (20)
\end{aligned}$$

$$\begin{aligned}
&\langle \boldsymbol{p}_1 s_1; \boldsymbol{p}_2 s_2 | J^\mu_b | \boldsymbol{P} \lambda_d \rangle \\
&= -\sum_{\sigma_2} \mathcal{P} \int \frac{d^3k_2}{(2\pi)^3} \frac{m}{E_{k_2}} \frac{m}{E_{P+q-k_2}} \\
&\quad \times \frac{1}{P^0 + \nu - E_{k_2} - E_{P+q-k_2}} \bar{u}_a(\boldsymbol{p}_1, s_1)\bar{u}_b(\boldsymbol{p}_2, s_2) \\
&\quad \times M_{ab;cd}(p_1, p_2; k_2) u_d(\boldsymbol{k}_2, \sigma_2)(\Lambda^+(\boldsymbol{P} + \boldsymbol{q} - \boldsymbol{k}_2) \\
&\quad \times \Gamma^\mu(q)\psi_{\lambda_d,\sigma_2}(k_2, P))_c, \quad (21)
\end{aligned}$$

and

$$\begin{aligned}
&\langle \boldsymbol{p}_1 s_1; \boldsymbol{p}_2 s_2 | J^\mu_c | \boldsymbol{P} \lambda_d \rangle \\
&= \sum_{\sigma_2} \int \frac{d^3k_2}{(2\pi)^3} \frac{m}{E_{k_2}} \frac{m}{E_{P+q-k_2}} \frac{1}{P^0 + \nu - E_{k_2} + E_{P+q-k_2} - i\epsilon} \\
&\quad \times \bar{u}_a(\boldsymbol{p}_1, s_1)\bar{u}_b(\boldsymbol{p}_2, s_2) M_{ab;cd}(p_1, p_2; k_2) u_d(\boldsymbol{k}_2, \sigma_2) \\
&\quad \times (\Lambda^-(\boldsymbol{k}_2 - \boldsymbol{q} - \boldsymbol{P})\Gamma^\mu(q)\psi_{\lambda_d,\sigma_2}(k_2, P))_c. \quad (22)
\end{aligned}$$

These contributions are represented by the diagrams in Fig. 2.

Equation (20), represented by Fig. 2(a), has all four legs of the pn scattering amplitude on-mass-shell. For this case, the scattering amplitude can be parametrized in terms of five Fermi invariants as

$$\begin{aligned}
M_{ab;cd} &= \mathcal{F}_S(s, t)\delta_{ac}\delta_{bd} + \mathcal{F}_V(s, t)\gamma_{ac} \cdot \gamma_{bd} \\
&\quad + \mathcal{F}_T(s, t)\sigma^{\mu\nu}_{ac}(\sigma_{\mu\nu})_{bd} + \mathcal{F}_P(s, t)\gamma^5_{ac}\gamma^5_{bd} \\
&\quad + \mathcal{F}_A(s, t)(\gamma^5\gamma)_{ac} \cdot (\gamma^5\gamma)_{bd}, \quad (23)
\end{aligned}$$

where s and t are the usual Mandelstam variables. The calculation of the invariant functions from helicity amplitudes is described in the Appendix. We use the helicity amplitudes

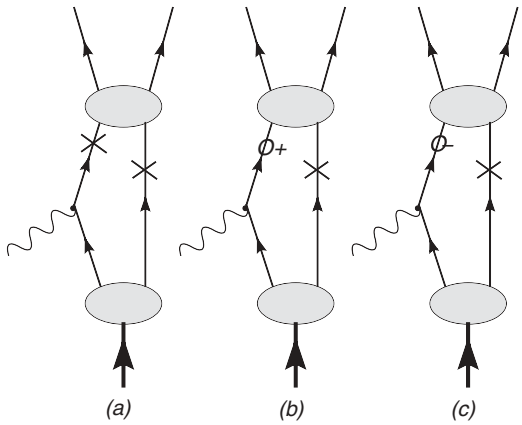

FIG. 2. Diagrams representing $\langle \boldsymbol{p}_1 s_1; \boldsymbol{p}_2 s_2 | J^\mu_a | \boldsymbol{P} \lambda_d \rangle$, $\langle \boldsymbol{p}_1 s_1; \boldsymbol{p}_2 s_2 | J^\mu_b | \boldsymbol{P} \lambda_d \rangle$, and $\langle \boldsymbol{p}_1 s_1; \boldsymbol{p}_2 s_2 | J^\mu_c | \boldsymbol{P} \lambda_d \rangle$. The insertion of a cross on an internal propagator indicates that the particle has been placed on the positive-energy mass shell. The insertion of $O+$ indicates that the positive-energy principal value part of the propagator is used, and the insertion of $O-$ indicates the negative-energy part of the propagator is used.

available from the Scattering Analysis Interactive Dial-in (SAID) program as input for our calculations [34]. For this calculation, we have constructed a table of the invariant functions in terms of s and the center of momentum angle θ. The table is then interpolated to obtain the invariant functions at the values required by the integration.

An alternative two-dimensional representation of the scattering amplitudes is in terms of the Saclay amplitudes. In this case, the scattering amplitude as an operator in two-dimensional spinor space is given by

$$\begin{aligned}\widetilde{M} = \tfrac{1}{2}[&(a_s + b_s) + (a_s - b_s)\boldsymbol{\sigma}_1 \cdot \hat{\boldsymbol{n}}\boldsymbol{\sigma}_2 \cdot \hat{\boldsymbol{n}} \\ &+ (c_s + d_s)\boldsymbol{\sigma}_1 \cdot \hat{\boldsymbol{m}}\boldsymbol{\sigma}_2 \cdot \hat{\boldsymbol{m}} + (c_s - d_s)\boldsymbol{\sigma}_1 \cdot \hat{\boldsymbol{l}}\boldsymbol{\sigma}_2 \cdot \hat{\boldsymbol{l}} \\ &+ e_s(\boldsymbol{\sigma}_1 + \boldsymbol{\sigma}_2) \cdot \hat{\boldsymbol{n}}],\end{aligned} \tag{24}$$

where

$$\hat{\boldsymbol{l}} = \frac{\boldsymbol{p}' + \boldsymbol{p}}{|\boldsymbol{p}' + \boldsymbol{p}|}, \quad \hat{\boldsymbol{m}} = \frac{\boldsymbol{p}' - \boldsymbol{p}}{|\boldsymbol{p}' - \boldsymbol{p}|}, \quad \hat{\boldsymbol{n}} = \frac{\boldsymbol{p} \times \boldsymbol{p}'}{|\boldsymbol{p} \times \boldsymbol{p}'|}, \tag{25}$$

for $\boldsymbol{p}$ and $\boldsymbol{p}'$ as the initial and final momenta of the proton. The first term is the central contribution, the next three terms are double-spin-flip terms, and the final term is a single-spin-flip term. We can determine the sensitivity of the $(e, e'p)$ observables to these terms by determining the Saclay amplitudes a_s, b_s, c_s, d_s, and e_s from the helicity matrix elements as described in the Appendix, setting some of the amplitudes to zero and then transforming the result to give new invariant amplitudes for the Fermi form. A common approximation is to use only the central part of the amplitude generated from a prescription involving the total cross section.

The contribution to the current matrix element given by Eq. (21), represented by Fig. 2(b), involves a principal value integral over off-mass-shell momenta for one leg of the scattering amplitude. The proton propagator for this leg contains only the positive-energy contribution. Determination of the off-shell behavior of the scattering amplitude requires a dynamical model of the amplitude. Such a model is not currently available to us in the range of energies required for the experiments being performed at Jefferson Lab. To estimate the possible effects of this contribution to the current matrix elements, we use a simple prescription for the off-shell behavior of the amplitude. Although additional invariants are possible when the nucleon is allowed to go off-shell, we keep only the forms in Eq. (23). The center-of-momentum angle is calculated using

$$\cos\theta = \frac{t - u}{\sqrt{s - 4m^2}\sqrt{\frac{(4m^2 - t - u)^2}{s} - 4m^2}}. \tag{26}$$

The invariants are then replaced by

$$\mathcal{F}_i(s, t) \to \mathcal{F}_i(s, t, u) F_N(s + t + u - 3m^2), \tag{27}$$

where

$$F_N(p^2) = \frac{\left(\Lambda_N^2 - m^2\right)^2}{(p^2 - m^2)^2 + \left(\Lambda_N^2 - m^2\right)^2}, \tag{28}$$

and the $\mathcal{F}_i(s, t, u)$ are obtained from interpolation of the on-shell invariant functions with the center-of-momentum angle obtained from Eq. (26). The form factor (28) was used as a cutoff in calculating the Gross vertex function used in this paper with $\Lambda_N = 1.675$ GeV. However, there should be an intrinsic falloff of the scattering amplitude due to the dynamics of the scattering which would be expected to be faster than provided by this cutoff mass. Figure 3 shows the off-shell form factor for cutoff masses of $\Lambda_N = 1.0$, 1.1, and 1.2 GeV. In the absence of a dynamical model of the scattering amplitudes, the effect of possible off-shell contributions on various observables can be reasonably estimated by using cutoff masses in this range.

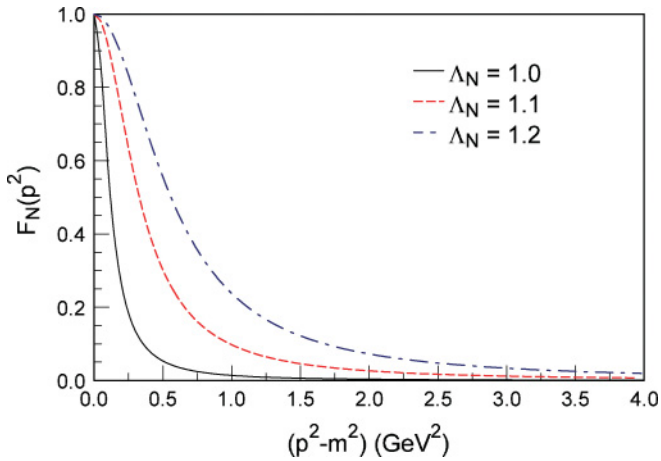

FIG. 3. (Color online) Off-shell nucleon form factor for $\Lambda_N = 1.0$, 1.1, and 1.2 GeV.

The contribution to the current matrix elements from Eq. (22), represented by Fig. 2(c), contains the effect of negative-energy propagation of the off-shell leg of the scattering amplitude. Since the denominator of this part of the propagator will be large compared with that of the positive-energy part at large momentum transfers, we neglect this contribution for the present. This is the only approximation involved in our calculation. Note, however, that by dropping this contribution the current matrix elements are no longer covariant. We have chosen to calculate the matrix elements in the laboratory frame.

A. Differential cross section

The ^{2}H$(e, e'p)$ cross section for unpolarized deuterons and protons in the laboratory frame can be written as [35,36]

$$\begin{aligned}\left(\frac{d\sigma^5}{d\epsilon' d\Omega_e d\Omega_p}\right)_h = \frac{m_p m_n p_p}{8\pi^3 M_d}\sigma_{\text{Mott}} f_{\text{rec}}^{-1}[&(v_L R_L + v_T R_T \\ &+ v_{TT} R_{TT}\cos 2\phi_p + v_{LT} R_{LT}\cos\phi_p) \\ &+ h v_{LT'} R_{LT'}\sin\phi_p],\end{aligned} \tag{29}$$

where M_d, m_p, and m_n are the masses of the deuteron, proton, and neutron, $p_p = p_1$ and Ω_p are the momentum and solid angle of the ejected proton, ϵ' is the energy of the detected electron, and Ω_e is its solid angle. The helicity of the electron is denoted by h. The Mott cross section is

$$\sigma_{\text{Mott}} = \left(\frac{\alpha\cos(\theta_e/2)}{2\varepsilon\sin^2(\theta_e/2)}\right)^2, \tag{30}$$

and the recoil factor is given by

$$f_{\rm rec} = \left| 1 + \frac{\omega p_p - E_p q \cos\theta_p}{M_d p_p} \right|. \tag{31}$$

The kinematic coefficients v_K are

$$v_L = \frac{Q^4}{q^4}, \tag{32}$$

$$v_T = \frac{Q^2}{2q^2} + \tan^2\frac{\theta_e}{2}, \tag{33}$$

$$v_{TT} = -\frac{Q^2}{2q^2}, \tag{34}$$

$$v_{LT} = -\frac{Q^2}{\sqrt{2}q^2}\sqrt{\frac{Q^2}{q^2} + \tan^2\frac{\theta_e}{2}}, \tag{35}$$

$$v_{LT'} = -\frac{Q^2}{\sqrt{2}q^2}\tan\frac{\theta_e}{2}. \tag{36}$$

If the response tensor is defined as

$$W^{\mu\nu} = \frac{1}{3}\sum_{s_1,s_2,\lambda_d} \langle \boldsymbol{p}_1 s_1; \boldsymbol{p}_2 s_2 | J^\mu | \boldsymbol{P}\lambda_d\rangle^* \langle \boldsymbol{p}_1 s_1; \boldsymbol{p}_2 s_2 | J^\nu | \boldsymbol{P}\lambda_d\rangle, \tag{37}$$

the response functions R_K are defined by

$$\begin{aligned} R_L &\equiv W^{00}, \\ R_T &\equiv W^{11} + W^{22} = w_{1,1} + w_{-1,-1}, \\ R_{TT}\cos 2\phi_p &\equiv W^{22} - W^{11} = 2\Re(w_{1,-1}), \\ R_{LT}\cos\phi_p &\equiv 2\sqrt{2}\Re(W^{01}) = -2\Re\left(w_1^0 - w_{-1}^0\right), \\ R_{LT'}\sin\phi_p &\equiv -2\sqrt{2}\Im(W^{02}) = -2\Re\left(w_1^0 + w_{-1}^0\right), \end{aligned} \tag{38}$$

where

$$\begin{aligned} w_{\lambda'_\gamma,\lambda_\gamma} = \frac{1}{3}\sum_{s_1,s_2,\lambda_d} &\langle \boldsymbol{p}_1 s_1; \boldsymbol{p}_2 s_2 | J_{\lambda'_\gamma} | \boldsymbol{P}\lambda_d\rangle^* \\ &\times \langle \boldsymbol{p}_1 s_1; \boldsymbol{p}_2 s_2 | J_{\lambda_\gamma} | \boldsymbol{P}\lambda_d\rangle, \end{aligned} \tag{39}$$

and

$$w^0_{\lambda_\gamma} = \frac{1}{3}\sum_{s_1,s_2,\lambda_d} \langle \boldsymbol{p}_1 s_1; \boldsymbol{p}_2 s_2 | J^0 | \boldsymbol{P}\lambda_d\rangle^* \langle \boldsymbol{p}_1 s_1; \boldsymbol{p}_2 s_2 | J_{\lambda_\gamma} | \boldsymbol{P}\lambda_d\rangle, \tag{40}$$

with

$$J_{\pm 1} = \mp\frac{1}{\sqrt{2}}(J^1 \pm i J^2). \tag{41}$$

For our calculations, we chose the following kinematic conditions: The z axis is parallel to $\boldsymbol{q}$, and the missing momentum is defined as $\boldsymbol{p}_m \equiv \boldsymbol{q} - \boldsymbol{p}_1 = \boldsymbol{p}_2 = \boldsymbol{p}_n$.

B. Asymmetries

The representation of the cross section in terms of response functions is due to the mixed polarization of the virtual photon which varies with the electron kinematics and polarization. The transverse-transverse response function is the result of interference between the $\lambda_\gamma = \pm 1$ helicity states, while the longitudinal-transverse response functions R_{LT} and $R_{LT'}$ are the result of interference between the deuteron charge and two linear combinations of the $\lambda_\gamma = \pm 1$ helicity states. As an alternative to a complete separation of the cross section into response functions, the interference response functions can be accessed through linear combinations of differential cross sections to produce three interference asymmetries defined as

$$A_{TT} = \frac{v_{TT} R_{TT}}{v_L R_L + v_T R_T}, \tag{42}$$

$$A_{LT} = \frac{\sigma_0(0^\circ) - \sigma_0(180^\circ)}{\sigma_0(0^\circ) + \sigma_0(180^\circ)} = \frac{v_{LT} R_{LT}}{v_L R_L + v_T R_T + v_{TT} R_{TT}}, \tag{43}$$

and

$$A_{LT'} = \frac{\sigma_{+1}(90^\circ) - \sigma_{-1}(90^\circ)}{\sigma_{+1}(90^\circ) + \sigma_{-1}(90^\circ)} = \frac{v_{LT'} R_{LT'}}{v_L R_L + v_T R_T - v_{TT} R_{TT}}, \tag{44}$$

where, for conciseness,

$$\sigma_h(\phi_p) \equiv \left(\frac{d\sigma^5}{d\epsilon' d\Omega_e d\Omega_p}\right)_h. \tag{45}$$

Note that while A_{LT} can be obtained by measuring protons in the electron scattering plane symmetrically about the direction of the three-momentum transfer, the asymmetries A_{TT} and $A_{LT'}$ require measurements to be made out of the scattering plane. The asymmetry $A_{LT'}$ is defined as an electron single-spin asymmetry and can, therefore, be easily obtained by flipping the beam helicity. While R_L and R_T are independent of photon-helicity-dependent phases, the interference response functions are not. As a result, the interference response functions can be very sensitive to phase differences generated by nonnucleonic currents and final state interactions. This is particularly true of $R_{LT'}$ which can be shown to be zero in the plane wave impulse approximation (PWIA). The interference response function R_{LT} is very sensitive to the relativity included in the current operator because of the various interference contributions from the charge and transverse current operators [37].

The observable $A_{LT'}$ has recently been measured in Jefferson Lab's Hall B [17]. Because of the large solid-angle coverage in Hall B, and the averaging over ϕ_p, the transverse-transverse interference response that is multiplied with a factor of $\cos(2\phi_p)$ in the cross section drops out of the measured asymmetry $A_{LT'}$ [38]. Therefore, from now on in this paper, we calculate

$$A_{LT'}^{\rm Hall\,B} = \frac{v_{LT'} R_{LT'}}{v_L R_L + v_T R_T}. \tag{46}$$

The difference between the asymmetry calculated with and without R_{TT} is very small in practice because of the small size of the transverse-transverse response.

III. RESULTS

In this section, we discuss our numerical results for several observables. We will investigate the effect of the final state

interactions (FSIs), and in particular, we will point out the contributions of spin-dependent FSIs, both the single-spin-flip and the double-spin-flip contributions. We will also discuss the relative importance of on-shell and off-shell contributions to FSI.

A. Differential cross sections

1. Momentum distributions

The most natural observable to investigate is the differential cross section. In Fig. 4, our calculations are compared to the published ^{2}H$(e, e'p)$ data from Jefferson Lab's Hall A. The data from Ulmer *et al*. [20] are shown together with our PWIA, on-shell FSI, and full FSI curves as a function of the missing momentum p_m in Fig. 4(a). For all the calculations in the paper, we use the MMD [39] proton electromagnetic form factors. The data are presented as a reduced cross section, which is defined as

$$\sigma_{\text{reduced}} = \frac{d^5\sigma}{d\Omega_{e'} d\Omega_N \, dE_{e'}} \frac{M_d \, f_{\text{rec}}}{\sigma_{ep} m_p m_n p_p}. \tag{47}$$

At lower missing momenta, the effects of FSIs are small. For missing momenta larger than $p_m \approx 110$ MeV, the FSI effects become visible. First, the PWIA curve is slightly above the FSI results; then, at $p_m \approx 300$ MeV, the FSI curves become larger than the PWIA contribution. The agreement with the data is quite nice overall. The off-shell FSI is small and leads to final results a little below the data at larger missing momenta. This is a sensible result, as we do expect meson exchange currents (MECs) to play a role at the relatively low Q^2 at which these data were taken. Indeed, in Ref. [20], the calculation by Arenhovel [40] agreed with the data at large missing momenta after MEC contributions were included; the FSI-only calculation was a bit below the data.

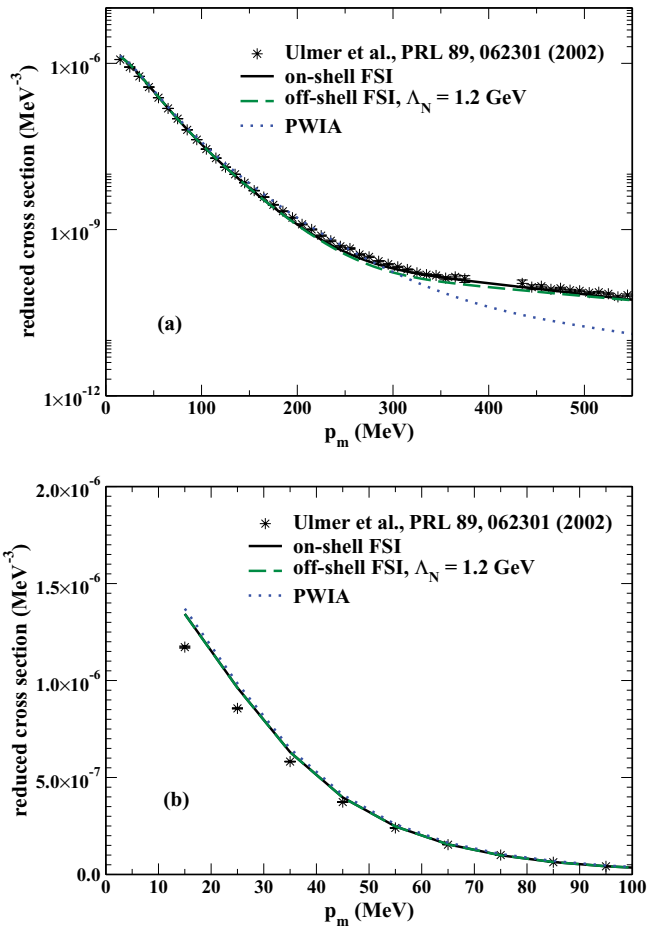

FIG. 4. (Color online) Reduced cross section for a beam energy of 3.1095 GeV, $Q^2 = 0.665\,\text{GeV}^2$, $x_{Bj} = 0.964$, and $\phi_p = 180^\circ$. The data are from Ref. [20].

We also have added a panel with a linear plot of just the low missing momentum data, see Fig. 4(b). The full FSI curve and the on-shell FSI curve coincide in this region. It has been observed in several previous ^{2}H$(e, e'p)$ measurements that at very low missing momenta, the calculations are somewhat above the data. This is quite puzzling as at these low missing momenta, effects like FSIs, MECs, etc., are supposed to be small and well under control. For a nice compilation on this topic, see Ref. [21]. In Ref. [20], Fig. 1 shows the deviation of the reduced cross section data and the calculations. Here, we observe the same type of deviation at very low $p_m \leqslant 0.35$ MeV. The largest discrepancy appears at $p_m = 15$ MeV, where our calculation overpredicts the data by 15%. Overall, comparing with the previous results, our low missing momentum results seem to be an improvement, even though the discrepancy has not been fully removed. One main difference between the calculation presented in this article and the calculations in Ref. [20] is the fully relativistic approach we take here.

Figure 5(a) shows the cross section as a function of the missing momentum, with a beam energy of 5.5 GeV, $Q^2 = 2\,\text{GeV}^2$, $x_{Bj} = 1$, and $\phi_p = 180^\circ$. The choice of Bjorken-x implies roughly quasifree kinematics. The azimuthal angle of the detected proton has been chosen to maximize the cross section. The PWIA and on-shell FSI curves are almost identical at very low missing momenta, up to 0.05 GeV. Then, the FSI curve reduces the cross section compared to the PWIA result, roughly from $p_m = 0.05$ to $p_m = 0.33$ GeV. For larger missing momenta, there is a marked increase in the differential cross section when FSI is included. These results are quite typical and have been seen in other calculations [23,25,26,41]. The differential cross section decreases by several orders of magnitude with increasing missing momentum, and a small reduction due to FSI at lower missing momenta and larger differential cross section can lead to a very large increase at larger missing momenta and smaller differential cross sections. The inclusion of the off-shell FSI contributions leads to a slight reduction of the cross section for medium missing momenta.

Figure 5(b) shows the ratios of the off-shell FSI calculations with $\Lambda_N = 1.0$, 1.1, and 1.2 GeV to the on-shell FSI. The off-shell effects are small for small p_m, but become increasingly large as p_m increases. These effects are not particularly sensitive to the cutoffs chosen here, but must be quite sensitive to lower cutoff masses.

In Fig. 6, we investigate the role played by the various parts of the proton-neutron scattering amplitude contributing to Eq. (23). The dashed line shows the results without the three double-spin-flip terms in the amplitude. One can see that for missing momenta from 0.2 to 0.45 GeV, the

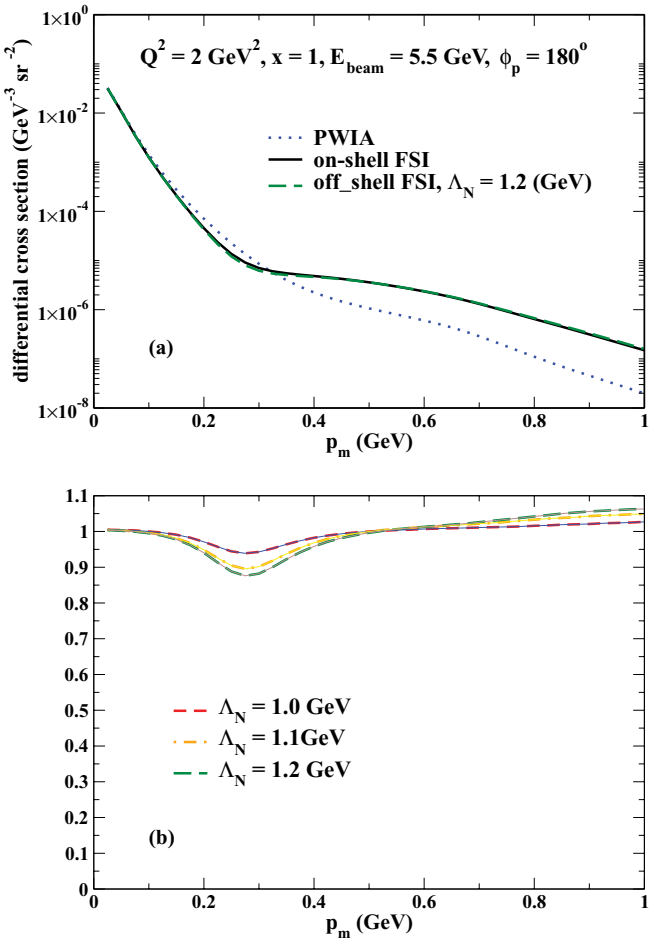

FIG. 5. (Color online) (a) Differential cross section for a beam energy of 5.5 GeV, $Q^2 = 2\,\mathrm{GeV}^2$, $x_{Bj} = 1$, and $\phi_p = 180^\circ$ in PWIA (dotted curve), with on-shell FSI (solid curve), and with on-shell and off-shell FSIs (dashed curve), as a function of the missing momentum. (b) Ratio of the off-shell calculations with varying cutoff $\Lambda_N = 1$ GeV (short-dashed), 1.1 GeV (dash-dotted), and 1.2 GeV (long-dashed) to the on-shell FSI calculation, in the same kinematics as (a).

double-spin-flip contribution is quite relevant. Its omission in this region leads to a significantly smaller cross section. The single-spin-flip (or spin-orbit) part of the proton-neutron scattering amplitude becomes relevant only at higher missing momenta than the double-spin-flip terms. From roughly $p_m = 0.3$ GeV on, omitting the spin-orbit contribution leads to a decrease in the differential cross section.

This clearly shows that while it is possible to parametrize the central part of the NN scattering amplitude and to reproduce the NN cross section data this way, this type of parametrization effectively includes some physics that stems from the spin-dependent parts of the NN amplitude. Here, it is interesting to see the influence of the spin-dependent parts of the NN amplitude on the unpolarized cross section. While the logarithmic scale necessary for the momentum distribution conceals the effects, it is important to note that the relative importance of the spin-dependent FSI contributions changes with missing momentum. We will return to the effects of spin-dependent FSI with Fig. 10.

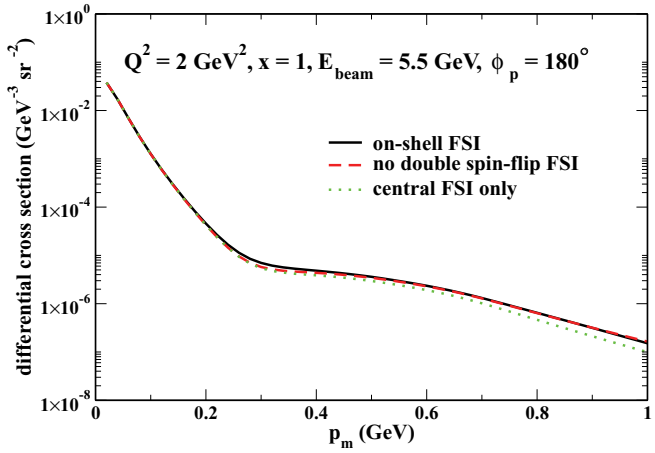

FIG. 6. (Color online) Differential cross section for a beam energy of 5.5 GeV, $Q^2 = 2\,\mathrm{GeV}^2$, $x_{Bj} = 1$, and $\phi_p = 180^\circ$ calculated with on-shell FSI, as a function of the missing momentum. The solid line shows the result calculated with the full NN scattering amplitude, the dashed line shows the result without the double-spin-flip terms of the NN scattering amplitudes, and the dotted line shows the result with the central NN amplitude only.

In Fig. 7, we display our results for the same four-momentum transfer, but higher $x_{Bj} = 1.3$. At this value of x_{Bj}, and larger values, strong short-range pn correlations have been reported by inclusive electron scattering experiments on deuterium [15,42]. The deviation of the on-shell FSI from the PWIA is small for medium missing momenta, and it seems to disappear altogether for missing momenta between 0.5 and 0.6 GeV. However, the off-shell contribution to the FSI gains in relevance for larger missing momenta and leads to a significant increase over the PWIA results at $p_m > 0.4$ GeV. Figure 7(b) again shows the ratio of off-shell FSI to the on-shell result for three values of the off-shell cutoff. The importance of the off-shell FSI here is larger than for $x_{Bj} = 1$ (as discussed above when considering Fig. 5) and the sensitivity to the value of the cutoff is much greater. This is the expected behavior, as the deviation from $x_{Bj} = 1$ corresponds to a deviation from the quasielastic kinematics and stresses the off-shell region more. A recent new proposal [18] suggests a measurement of the cross section at somewhat larger $Q^2 = 3.5\,\mathrm{GeV}^2$, but the same value of $x_{Bj} = 1.3$ and a beam energy of $E_{\mathrm{beam}} = 5.25$ GeV. The results of our calculation for these kinematics are similar to what is displayed in Fig. 7. The on-shell FSI in this case deviates a bit more from the PWIA result than for the kinematics displayed here. The off-shell contribution is just as significant in the proposed kinematics.

2. *Angular distributions*

In Figure 8, we show the cross section as a function of the angle θ_m of the missing momentum, with fixed $Q^2 = 2\,\mathrm{GeV}^2$ and $p_m = 0.4$ GeV. The beam energy and azimuthal angle of the proton are the same as for the momentum distribution graphs. The angular distribution of the cross section shows much less variation in the magnitude, and therefore it can be shown on a linear plot, allowing a better look at the

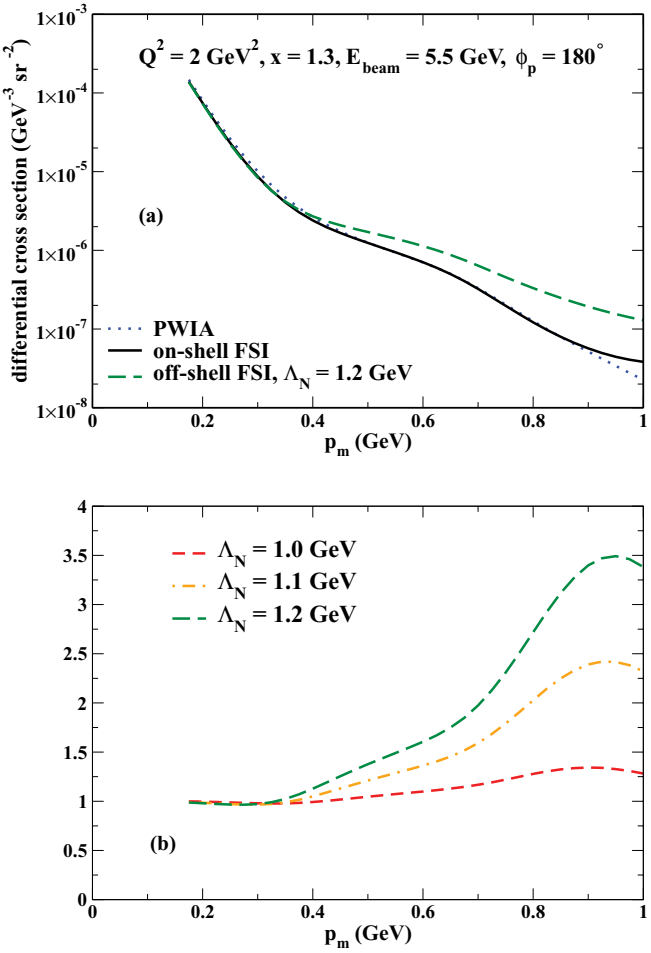

FIG. 7. (Color online) (a) Differential cross section for a beam energy of 5.5 GeV, $Q^2 = 2\,\mathrm{GeV}^2$, $x_{Bj} = 1.3$, and $\phi_p = 180^\circ$ in PWIA (dotted curve), with on-shell FSI (solid curve), and with on-shell and off-shell FSIs (dashed curve), as a function of the missing momentum. (b) Ratio of the off-shell calculations with varying cutoff $\Lambda_N = 1$ GeV (short-dashed), 1.1 GeV (dash-dotted), and 1.2 GeV (long-dashed) to the on-shell FSI calculation, in the same kinematics as (a).

relevance of various parts of the cross section. While the region beyond $\theta_m = 80^\circ$ is kinematically accessible to experiment, a calculation in this region requires the knowledge of the NN scattering amplitude above laboratory kinetic energies of 1.3 GeV in the pn system, which are not available from SAID. We therefore stay below 80°. As is obvious from the plot, the most interesting features of the calculation are located below this angle: while the PWIA results are gently sloping upward and then downward for angles larger than 20°, the FSI results initially follow this behavior, but then show a pronounced peak at around $\theta_m = 70^\circ$. This value corresponds to $x_{Bj} = 1$, i.e., quasifree kinematics for the knocked-out nucleon. For the lower angles, the FSI simply leads to a reduction in the cross section, but the shape is unchanged. For larger angles, around $x_{Bj} = 1$, the diffractive nature of the FSI leads to a redistribution of strength from smaller missing momenta, causing a large peak.

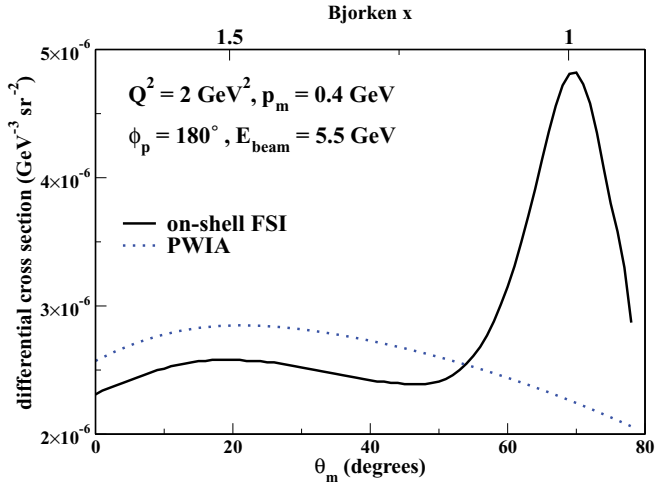

FIG. 8. (Color online) Differential cross section for a beam energy of 5.5 GeV, $Q^2 = 2\,\mathrm{GeV}^2$, $p_m = 0.4$ GeV, and $\phi_p = 180^\circ$ in PWIA (dotted curve) and with on-shell FSI (solid curve), as a function of the angle of the missing momentum. The top axis shows the corresponding values of Bjorken-x.

If we consider the ratio of FSI to PWIA cross section, as is sometimes done when comparing various methods of calculation [21,23], this ratio peaks at 70°, too. Our calculation clearly shows the same shift from a peak at 90°, as seen in Glauber theory calculations [43], to a lower angle, as seen in the generalized eikonal approximation (GEA) [23] and the diagrammatic approach of Laget [26].

For the angular distribution, the influence of the off-shell FSI cutoff is clearly visible and can be studied easily. One does not expect a large contribution from far off-shell nucleons. The cutoff we use here serves to impose that constraint. For the kinematics displayed in Fig. 9, we investigate the effects of various cutoff values. The cutoff at 1 GeV leads to a very small increase at small angles and a very small decrease at large angles, but the overall result is hardly different from the

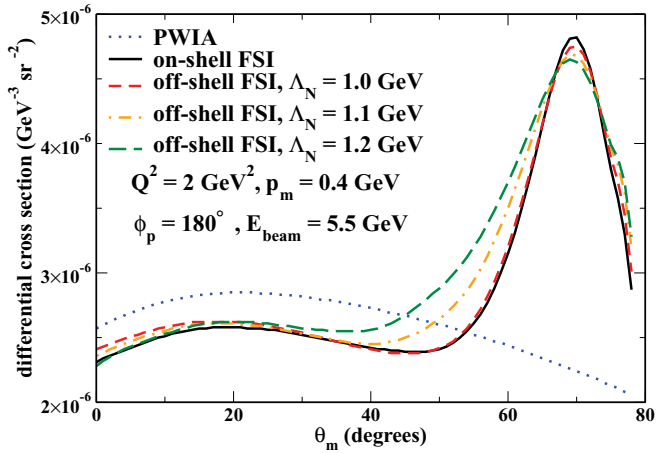

FIG. 9. (Color online) Differential cross section for a beam energy of 5.5 GeV, $Q^2 = 2\,\mathrm{GeV}^2$, $p_m = 0.4$ GeV, and $\phi_p = 180^\circ$ with on-shell FSI (solid curve) and with on-shell and off-shell FSIs at various cutoffs, as a function of the angle of the missing momentum.

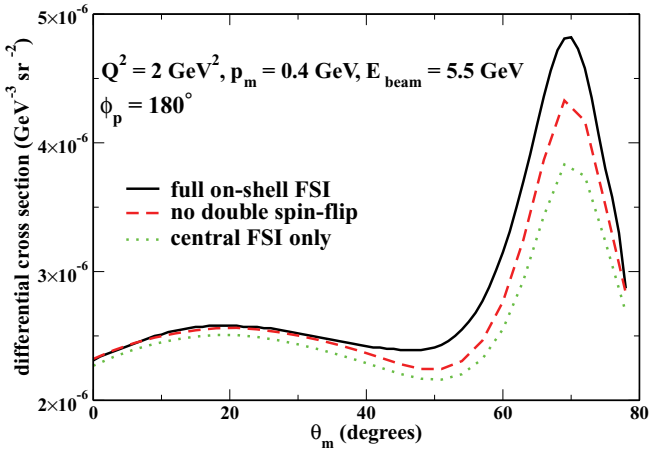

FIG. 10. (Color online) Differential cross section for a beam energy of 5.5 GeV, $Q^2 = 2\,\mathrm{GeV}^2$, $p_m = 0.4$ GeV, and $\phi_p = 180^\circ$ calculated with on-shell FSI, as a function of the angle of the missing momentum. The solid line shows the result calculated with the full NN scattering amplitude, the dashed line shows the result without the double-spin-flip terms of the NN scattering amplitudes, and the dotted line shows the result with the central NN amplitude only.

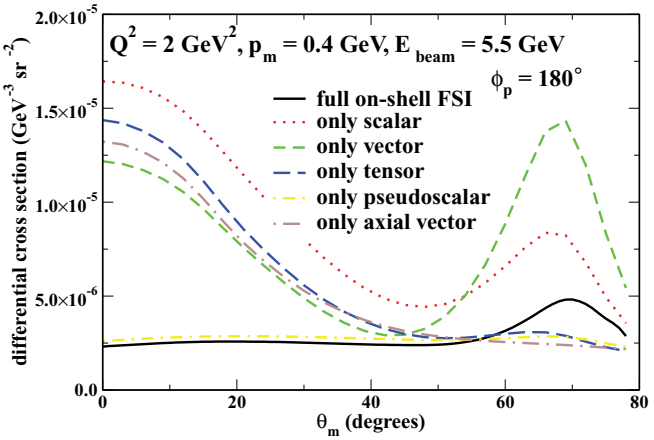

FIG. 11. (Color online) Differential cross section for a beam energy of 5.5 GeV, $Q^2 = 2\,\mathrm{GeV}^2$, $p_m = 0.4$ GeV, and $\phi_p = 180^\circ$ with on-shell FSI as a function of the angle of the missing momentum. The solid curve shows the contribution of the full NN scattering amplitude, the other curves show the results for just one invariant term in the NN scattering amplitude.

on-shell FSI-only result. The primary effect for larger cutoff masses is to fill in the minimum in the on-shell result from 30° to 65°.

In Fig. 10, we show the effects of the various spin-dependent parts of the pn scattering amplitude. It is very interesting to observe that in the peak region, the contribution of the spin-dependent FSIs (both single- and double-spin-flip) amounts to about one-quarter of the cross section. This is certainly a rather significant contribution. The contribution from the single-spin-flip term and the three double-spin-flip terms is about equal in the peak region. The figure shows that the double-spin-flip contribution to the cross section at small angles is almost negligible. It becomes noticeable at $\theta_m \approx 40^\circ$ and then leads to a sizable increase of the differential cross section in the peak region. The omission of the single-spin-flip contribution leads to a noticeable reduction in the cross section for all angles. The effect is most pronounced in the peak region and in the very shallow dip just before the peak region.

To this point, we have considered the different contributions of the spin-dependent parts of the amplitude, i.e., of the NN amplitude split up following the Saclay convention [Eq. (24)]. Using the Saclay formalism with its classification according to the spin dependence is quite useful, as it allows one to understand the new contributions from different parts of the current operator when adding the single-spin-flip term and the double-spin-flip terms, see Ref. [41]. Even though we did not rewrite our current operator to distinguish, e.g., between magnetization current and convection current, seeing the NN scattering amplitude in terms of its spin dependence is a very natural viewpoint and allows a certain intuitive understanding of the numerical results.

It is also interesting to investigate the NN amplitude in terms of the five Fermi invariants, which are so practical for actual calculations. From Eqs. (A8) and (A22), it is clear that every invariant amplitude contains several different spin-dependent pieces. In Fig. 11, we show the results of the calculation with on-shell FSI if only one of the five invariants is included. For comparison, the solid line depicts the result obtained with the full NN amplitude. The result obtained with just the pseudoscalar part is slightly above the full result for smaller angles, and it continues smooth and almost straight toward larger angles. It does not exhibit a peak structure at large angles. The tensor and axial vector contributions are fairly close to the pseudoscalar contribution at large angles, and neither exhibits a peak at large angles. At small angles, however, these two contributions lead to a new peak, much larger than the original peak at large angles in the full result. The scalar and vector contributions show peaks at small angles and a large peak at large angles. These results already show that there are large interference effects present between the various invariant amplitudes. There is no straightforward and intuitive explanation available for why these contributions interfere in such a way.

In Fig. 12, we show the angular distribution of the differential cross section for a lower missing momentum, $p_m = 0.2$ GeV. The lower missing momentum implies that the limiting value of 1.3 GeV laboratory energy for the NN system is reached at larger angles than for $p_m = 0.4$ GeV. While the PWIA curve here is very similar in shape to the curve at the higher missing momentum value, the FSI curve looks rather different now. Instead of a fairly sharp peak around $\theta_m = 70^\circ$, we now observe a broad, shallow dip at larger angles. At lower missing momenta, the FSIs lead to a reduction in the cross section. Part of this strength is redistributed to larger missing momenta, as discussed above. Also including the off-shell FSIs has no effect at very small angles, roughly below 20°, and then tends to shift the overall result toward lower angles.

In Fig. 13, the influence of the different kinds of FSIs is shown at low missing momentum. Switching off the double-spin-flip contribution leads to a small reduction in the cross section for medium and large angles, roughly 5% in the region

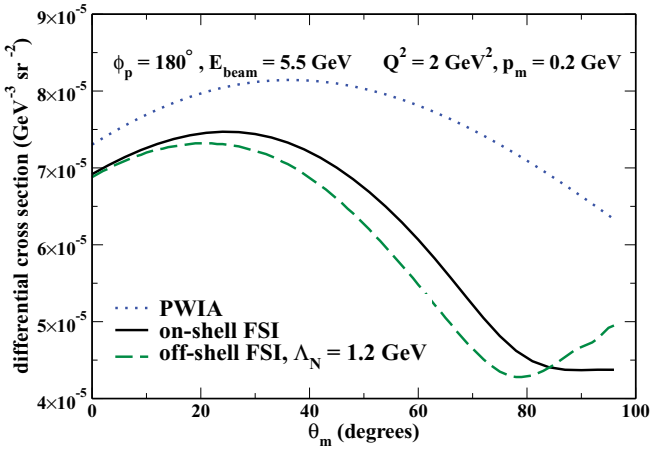

FIG. 12. (Color online) Differential cross section for a beam energy of 5.5 GeV, $Q^2 = 2\,\mathrm{GeV}^2$, $p_m = 0.2$ GeV, and $\phi_p = 180^\circ$ in PWIA (dotted curve), with on-shell FSI (solid curve), and with on-shell and off-shell FSIs (dashed curve), as a function of the angle of the missing momentum.

of the shallow dip. Switching off the single-spin-flip term, too, changes practically nothing. The FSIs in this kinematic region are overall smaller than for higher missing momenta. The influence of spin-dependent FSIs is smaller here, too. However, it is interesting to note that the double-spin-flip terms are actually more relevant here than the single-spin-flip terms. We have observed this already when discussing the momentum distributions shown in Fig. 6.

B. Asymmetries

Figure 14 shows the interference asymmetry A_{TT} for $Q^2 = 2.0$ GeV and $E_{\mathrm{beam}} = 5.5$ GeV. Figure 14(a) is for $x_{Bj} = 1$, and 14(b) is for $x_{Bj} = 1.3$.

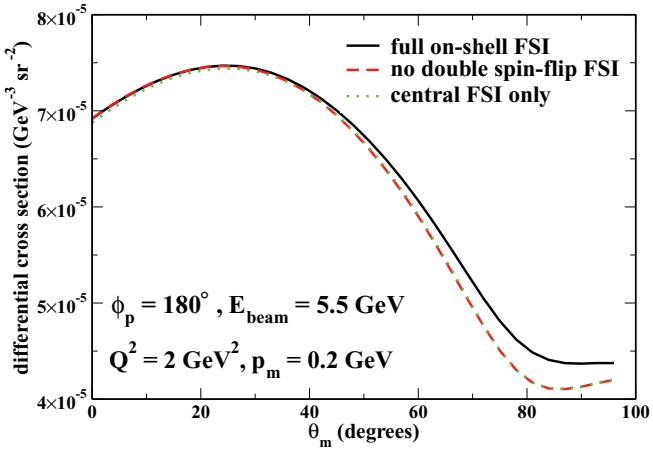

FIG. 13. (Color online) Differential cross section for a beam energy of 5.5 GeV, $Q^2 = 2\,\mathrm{GeV}^2$, $p_m = 0.2$ GeV, and $\phi_p = 180^\circ$ calculated with on-shell FSI, as a function of the angle of the missing momentum. The solid line shows the result calculated with the full NN scattering amplitude, the dashed line shows the result without the double-spin-flip terms of the NN scattering amplitudes, and the dotted line shows the result with the central NN amplitude only.

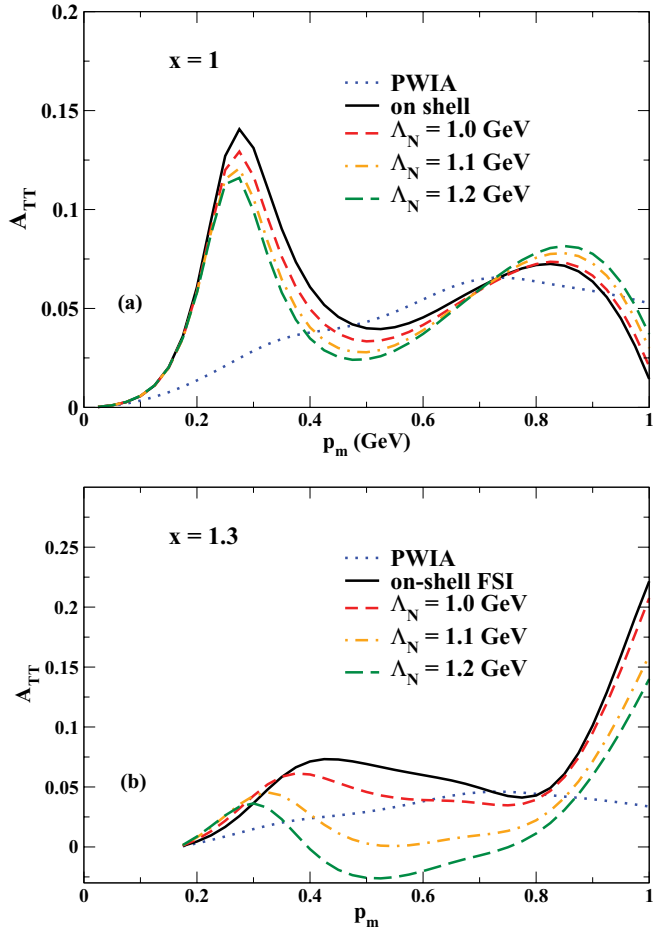

FIG. 14. (Color online) (a) Asymmetry A_{TT} for $x_{Bj} = 1$ in PWIA (dotted line), with on-shell FSI (solid line), and with off-shell FSI for various values of the cutoff. (b) Same as (a), but for $x_{Bj} = 1.3$.

In both cases, the FSI results in a substantial change from the PWIA result, with respect to both the size and shape of the asymmetry. For $x_{Bj} = 1$, the variation with the cutoff mass for the three values shown here is small, but it is somewhat larger for $x_{Bj} = 1.3$, reducing the asymmetry almost to zero for $\Lambda_N = 1.2$ GeV around $p_m = 0.5$ GeV.

Figure 15 shows results for the interference asymmetry A_{LT} for the same kinematics as in the previous figure. Again the sensitivity to final state interactions is substantial. Sensitivity to off-shell contributions is relatively modest at $x_{Bj} = 1$ but is much larger at $x_{Bj} = 1.3$.

The single-spin asymmetry $A_{LT'}$ is shown in Fig. 16 for the same kinematics. This asymmetry is identically zero in the PWIA, so the FSIs are responsible for any asymmetry. A more detailed discussion of FSI effects is given below for kinematics relevant to a recent experiment. Here, in these kinematics, we focus on comparing the behavior of the three asymmetries, in the same kinematics.

At $x_{Bj} = 1$, there is very little sensitivity to off-shell contributions, but it is large at $x_{Bj} = 1.3$. As stated above, this behavior is expected, as $x_{Bj} = 1$ corresponds to quasifree, i.e., on-shell, kinematics, while $x_{Bj} = 1.3$ probes nucleons that

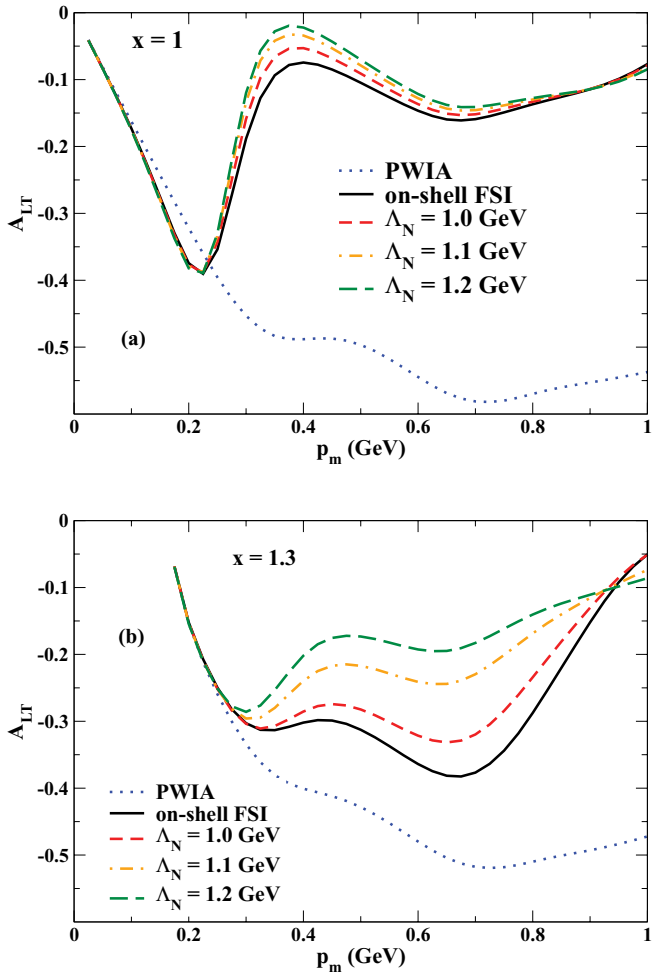

FIG. 15. (Color online) Same as Fig. 14, but for interference asymmetry A_{LT}.

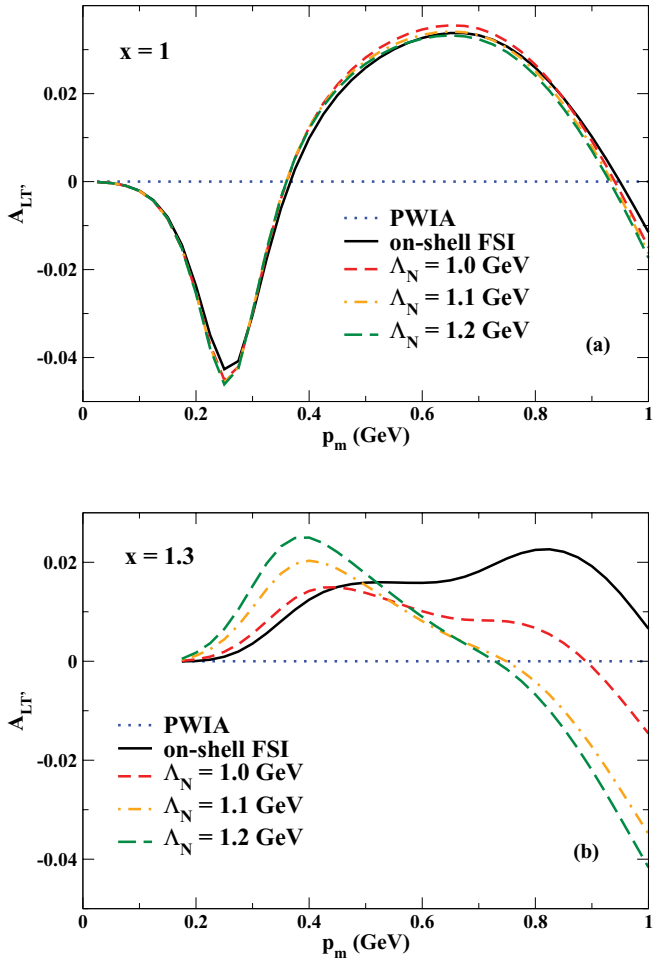

FIG. 16. (Color online) Same as Fig. 14, but for the asymmetry $A_{LT'}$.

are much more off-shell. From the plots for $x_{Bj} = 1.3$, one can see clearly that the off-shell contribution to the NN scattering amplitude introduces a certain amount of ambiguity, especially at medium to high missing momenta. While great progress has been made on the experimental side, with measurements at very high missing momenta, there clearly are some theoretical uncertainties in these kinematic regions.

We are in the fortunate situation that the asymmetry $A_{LT'}$ has been measured over a wide range of kinematics, from very low four-momentum transfers $Q^2 \approx 0.2\,\mathrm{GeV}^2$ up to medium values of $Q^2 \approx 1\,\mathrm{GeV}^2$ [17]. The data are currently under analysis. In this range, the proton-neutron scattering amplitudes from SAID are available, so there are no limits to our ability to calculate for these kinematics.

Here, we discuss our results for two representative kinematics: $Q^2 = 0.5\,\mathrm{GeV}^2$, and $Q^2 = 1.0\,\mathrm{GeV}^2$. In both cases, we assume a beam energy of 2.558 GeV. Figure 17 shows our results for $Q^2 = 1\,\mathrm{GeV}^2$. The PWIA result is zero and not shown on the plot. The full, on-shell FSI result starts out negatively, dips around $p_m \approx 0.25$ GeV, and then increases and changes sign around $p_m \approx 0.38$ GeV. Then, the asymmetry peaks around $p_m \approx 0.5$ GeV, and then decreases and changes sign again. The second zero of the asymmetry occurs at $p_m \approx 0.7$ GeV. One can see that the double-spin-flip contributions to the FSI are not very relevant; they just lead to small modifications in the dip and peak regions. The spin-orbit (i.e., the single-spin-flip) contribution is very important, though. Switching it off so that only the central FSI remains leads to a completely different picture: the asymmetry is tiny and remains positive for large missing momenta.

In Fig. 18, we show the corresponding results for the spin-dependence of the FSIs for lower four-momentum transfer, $Q^2 = 0.5\,\mathrm{GeV}^2$. At these kinematics, we do expect the influence of meson exchange currents and isobar states to be relevant. These effects are not included in the present calculation. However, the FSIs are crucial for $A_{LT'}$, and we can investigate them within our model. The full calculations are qualitatively very similar at both Q^2 values, showing a negative dip around $p_m \approx 0.25$ GeV and then an increase into positive values, with a peak around $p_m \approx 0.5$ GeV. A very interesting difference, however, is the size of the contribution of the double-spin-flip terms to the FSI. While their influence is small, almost negligible, at the higher Q^2 value, it is quite significant for the low Q^2 value: the double-spin-flip terms serve to partially fill in the negative dip, and they are also responsible for pushing the asymmetry back toward positive values.

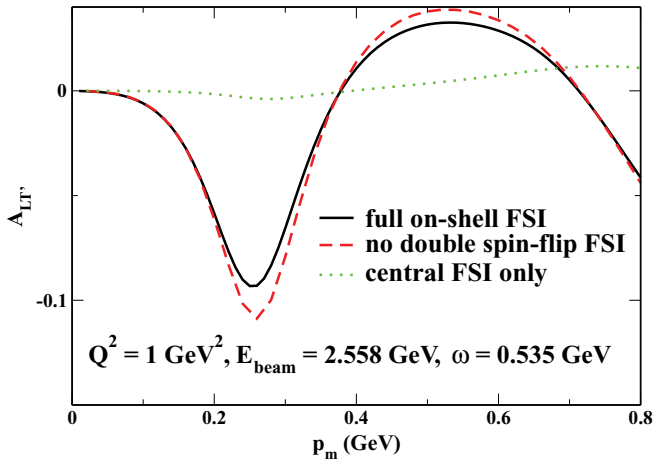

FIG. 17. (Color online) LT' asymmetry for a beam energy of 2.558 GeV and four-momentum transfer $Q^2 = 1\,\mathrm{GeV}^2$ calculated with on-shell FSI, as a function of the missing momentum. The solid line shows the result calculated with the full NN scattering amplitude, the dashed line shows the result without the double-spin-flip terms of the NN scattering amplitudes, and the dotted line shows the result with the central NN amplitude only.

C. FSI details

One obvious difference between the calculation presented here and the traditional Glauber and generalized eikonal approximation (GEA) is the evaluation of the argument of the nucleon-nucleon scattering amplitude for the FSIs. As described in Sec. II, we evaluate the five terms of the NN scattering amplitude in Eq. (23) at the values of the Mandelstam variables s and t computed from the particular kinematics. In Glauber and GEA settings, one typically finds expressions where the NN scattering amplitude is evaluated assuming a purely transverse momentum transfer when evaluating t, even though the longitudinal momentum transfer is taken into account in the GEA. This is typically denoted with expressions like $f_{NN}(k_\perp)$. With the kinematics variables as defined in Fig. 1, the Mandelstam t is given by $t = (M_d - E_{k_2} + \omega - E_{p_1})^2 - (\mathbf{p_1} + \mathbf{k_2} - \mathbf{q})^2$, whereas assuming a purely transverse momentum transfer implies $t_\perp = -(\mathbf{p_{1,\perp}} + \mathbf{k_{2,\perp}})^2$. Using this, we can define the c.m. scattering angle as

$$\cos\theta = 1 + \frac{2t_\perp}{s - 4m^2}. \tag{48}$$

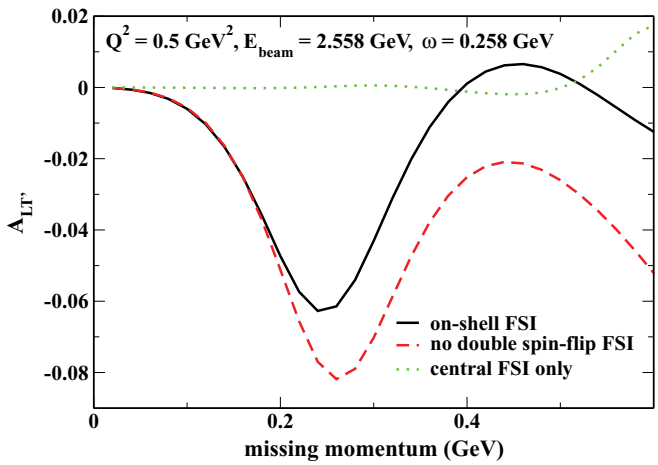

FIG. 18. (Color online) Same as Fig. 17, but for $Q^2 = 0.5\,\mathrm{GeV}^2$.

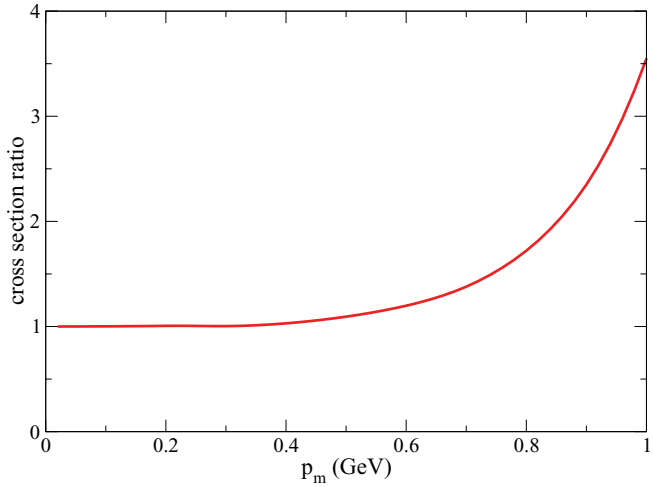

FIG. 19. (Color online) Ratio of the differential cross section evaluated with the full NN argument t and with the purely transverse momentum $t_\perp$. The kinematics are identical to Fig. 5: beam energy of 5.5 GeV, $Q^2 = 2\,\mathrm{GeV}^2$, $x_{Bj} = 1$, and $\phi_p = 180^\circ$. The calculation was performed using on-shell FSI.

In Fig. 19, we show the ratio of the transverse-momentum approximation to the full, on-shell calculation. The kinematics are identical to the kinematics used for Fig. 5: a beam energy of 5.5 GeV, $Q^2 = 2\,\mathrm{GeV}^2$, $x_{Bj} = 1$, and $\phi_p = 180^\circ$. Up to missing momenta of 0.4 GeV, the approximation works well, leading to small deviations of less than 5%. Beyond 0.4 GeV, the deviation from the full result grows; and for missing momenta larger than 0.6 GeV, the quality of the approximation deteriorates quickly.

We have performed the same calculation for the angular distribution shown in Fig. 8. Here, we found that the approximation does well; the deviations are less than 5% for any angle. This corresponds to our findings for the momentum distribution.

As an illustrative example of the other observables discussed in this article, we also show our results for the asymmetry $A_{LT'}$ in Fig. 20. The kinematics correspond to Fig. 17; we used a beam energy of 2.558 GeV and four-momentum transfer $Q^2 = 1\,\mathrm{GeV}^2$. The spike seen in the ratio around $p_m = 0.4$ GeV stems from the sign change in the asymmetry; it is not relevant to our discussion. Again, we see that the approximation is doing well up to missing momenta of roughly 0.4 GeV. Then, the approximation considerably overestimates the full result; and for very large missing momenta, $p_m \geqslant 0.7$ GeV, it even fails to reproduce the correct sign of the asymmetry. It is interesting to see that the effects of the approximation are visible even in a quantity that is a ratio of quantities that are both affected by the approximation.

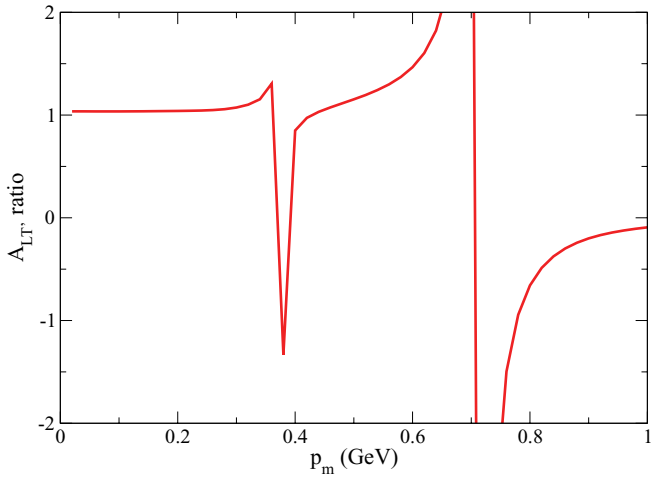

FIG. 20. (Color online) Ratio of the asymmetry $A_{LT'}$ evaluated with the full NN argument t and with the purely transverse momentum $t_\perp$. The kinematics are identical to Fig. 17; the calculations were performed using on-shell FSI.

In conclusion, approximating the argument of the NN scattering amplitude with the popular "transverse momentum transfer only" works well up to missing momenta of 0.4 GeV for various observables. For missing momenta higher than that, the approximation becomes questionable.

IV. SUMMARY AND OUTLOOK

In this paper, we have presented a fully relativistic ^{2}H$(e, e'p)$ calculation in impulse approximation. We steered clear of a number of common, simplifying assumptions. The only approximation made in this paper is neglecting the negative-energy contributions to the propagator of the off-shell nucleon. These contributions can realistically be expected to be very small compared to the positive-energy contributions.

We have used a parametrization of experimental NN data from SAID to describe the full pn scattering amplitude for the final state interaction. This leads to certain limits in the kinematics we can access, as these parametrizations are available only for laboratory kinetic energies of 1.3 GeV or less. In our calculations, we investigated the effects of the different contributions to the NN scattering amplitude: the central, spin-orbit, and double-spin-flip parts, using the Saclay formalism to describe the different contributions. Many other fine calculations using the generalized eikonal approximation [23–25] or a diagrammatic approach [26] use the central part only. While the central part of the amplitude is clearly dominant in almost all observables, the spin-orbit and double-spin-flip parts do contribute visibly to the cross section in the peak area of the angular distribution, increasing the peak height roughly by one-quarter. For the out-of-plane asymmetry $A_{LT'}$, which is nonzero only in the presence of FSIs, the spin-orbit part is clearly the most relevant. Depending on the kinematics, the double-spin-flip can also play a relevant role for this asymmetry.

We also showed the different contributions of the NN amplitude in terms of the five invariant amplitudes. Interestingly, they are all relevant, and a lot of interference effects contribute to the full result. It is not possible to identify a single dominant contribution in this framework for the description of the NN amplitudes.

In the spirit of avoiding all unnecessary approximations, we used the full argument for the calculation of the NN scattering amplitudes. In Glauber theory and its variants, one often encounters the assumption of a transverse momentum transfer only, and this changes the value of Mandelstam t. We investigated the validity of this assumption and found that it is a very good approximation for missing momenta up to 0.4 GeV. For higher missing momenta, the quality of this approximation deteriorates quickly, and it probably should not be used.

We have also compared the influence of the off-shell FSI contributions to the on-shell FSI contributions. The former are expected to not be too large, and they require some interpolation of on-shell amplitudes and the introduction of a regulator function to suppress very far off-shell contributions. The off-shell FSI contributions tend to be negligible to small for lower missing momenta, $p_m \leqslant 0.4$ GeV, for any observable. Beyond that, their importance varies depending on the specific kinematics: the off-shell FSI is very small for the momentum distribution calculated for the quasifree value $x_{Bj} = 1$, but it is large for $x_{Bj} = 1.3$. This pattern was observed both for the cross section and the asymmetries A_{TT}, A_{LT}, and $A_{LT'}$. The size of the off-shell contribution does depend on the chosen cutoff, with a larger cutoff admitting a sometimes much larger contribution. The main purpose of showing figures with the ratios of off-shell calculations with different cutoffs to the on-shell result is to identify "safe" kinematics and observables, where the off-shell FSI contributions are definitely small. In regions where they are relevant, a certain amount of theoretical uncertainty cannot be avoided, until reliable and believable models of the off-shell NN interaction at the relevant energies are developed. This is particularly relevant for the interpretation of new data taken at high missing momentum at Jefferson Lab.

The current calculations will be applied or already have been applied to the forthcoming experimental data from Jefferson Lab [14,17], and calculations for the BLAST data from MIT Bates [16] are planned. Our calculation also does a nice job of improving the agreement with the low missing momentum data of Ulmer *et al.* [20], even though the "low missing momentum puzzle" [21] is not completely resolved.

Logical next steps for enhancing our calculations are the inclusion of meson exchange currents and isobar states.

ACKNOWLEDGMENTS

We thank Paul Ulmer for quickly providing us with his data from Ref. [20] in tabulated form. SJ thanks Charlotte Elster for interesting discussions. This work was supported in part by the U.S. Department of Energy (DOE) under cooperative research agreement No. DE-AC05-06OR23177, and by the National Science Foundation under Grant Nos. PHY-0354916 and PHY-0653312. Work was also done by Jefferson Science Associates, LLC, under U.S. DOE Contract No. DE-AC05-06OR23177.

APPENDIX: REPRESENTATIONS OF THE *NN* AMPLITUDES

The invariant functions $\mathcal{F}_i(s,t)$ can be obtained from scattering data. For example, the helicity amplitudes are defined as

$$\mathcal{M}_{\lambda_1'\lambda_2';\lambda_1\lambda_2} = (\bar{u}_{\lambda_1'}(\boldsymbol{p}_1'))_a(\bar{u}_{\lambda_2'}(\boldsymbol{p}_2'))_b M_{ab,cd}(u_{\lambda_1}(\boldsymbol{p}_1))_c(u_{\lambda_2}(\boldsymbol{p}_2))_d, \quad \text{(A1)}$$

where $u_\lambda(\boldsymbol{p})$ is the helicity spinor for helicity λ. The helicity matrix elements for pn scattering in the center-of-momentum frame can be obtained from the SAID program for laboratory kinetic energies of up to 1.3 GeV. If the amplitudes are extracted in units of fm, the helicity amplitudes consistent with the conventions used here are related to the SAID amplitudes by

$$\mathcal{M}_{\lambda_1'\lambda_2';\lambda_1\lambda_2} = -\frac{4\pi\sqrt{s}}{\hbar c m^2}\mathcal{M}^{\text{SAID}}_{\lambda_1'\lambda_2';\lambda_1\lambda_2}. \quad \text{(A2)}$$

Parity, time-reversal, and particle interchange symmetries can be used to show that there are only five independent helicity amplitudes, defined as

$$a = \mathcal{M}_{1,1;1,1}, \quad \text{(A3)}$$

$$b = \mathcal{M}_{1,1;1,-1}, \quad \text{(A4)}$$

$$c = \mathcal{M}_{1,-1;1,-1}, \quad \text{(A5)}$$

$$d = \mathcal{M}_{1,1;-1,-1}, \quad \text{(A6)}$$

$$e = \mathcal{M}_{1,-1;-1,1}. \quad \text{(A7)}$$

Using Eq. (23) in Eq. (A1) and solving for the invariant functions gives

$$\begin{Bmatrix}\mathcal{F}_S\\ \mathcal{F}_V\\ \mathcal{F}_T\\ \mathcal{F}_P\\ \mathcal{F}_A\end{Bmatrix} = \frac{1}{s-4m^2}\begin{bmatrix}a_{11} & a_{12} & a_{13} & a_{14} & a_{15}\\ a_{21} & a_{22} & a_{23} & a_{24} & a_{25}\\ a_{31} & a_{32} & a_{33} & a_{34} & a_{35}\\ a_{41} & a_{42} & a_{43} & a_{44} & a_{45}\\ a_{51} & a_{52} & a_{53} & a_{54} & a_{55}\end{bmatrix}\begin{Bmatrix}a\\ b\\ c\\ d\\ e\end{Bmatrix}, \quad \text{(A8)}$$

where

$$a_{11} = -a_{24} = a_{25} = -2a_{31} = a_{41} = -a_{54} = -a_{55} = -\frac{2m^4}{s}, \quad \text{(A9)}$$

$$a_{14} = -a_{15} = -a_{21} = -2a_{34} = 2a_{35} = a_{44} = -a_{51} = \frac{2m^4}{s} - m^2, \quad \text{(A10)}$$

$$a_{12} = \frac{m[8m^2 - (3+\cos\theta)s]}{\sqrt{s}\sin\theta}, \quad \text{(A11)}$$

$$a_{13} = \frac{m^2[2m^2(1+\cos\theta) - s(3+\cos\theta)]}{s(1+\cos\theta)}, \quad \text{(A12)}$$

$$a_{22} = \frac{4m^2(1+\cos\theta)}{\sqrt{s}\sin\theta}, \quad \text{(A13)}$$

$$a_{23} = \frac{2m^2[m^2(1+\cos\theta) + s]}{s(1+\cos\theta)}, \quad \text{(A14)}$$

$$a_{32} = -\frac{m\sqrt{s}(1-\cos\theta)}{2\sin\theta}, \quad \text{(A15)}$$

$$a_{33} = -\frac{m^2[m^2(1+\cos\theta) + s(1-\cos\theta)]}{s(1+\cos\theta)}, \quad \text{(A16)}$$

$$a_{42} = -\frac{m[8m^2 + s(3+\cos\theta)]}{\sqrt{s}\sin\theta}, \quad \text{(A17)}$$

$$a_{43} = \frac{m^2[2m^2(1+\cos\theta) - s(3+\cos\theta)]}{s(1+\cos\theta)}, \quad \text{(A18)}$$

$$a_{45} = -\frac{m^2[2m^2(1-\cos\theta) + s(7+\cos\theta)]}{s(1-\cos\theta)}, \quad \text{(A19)}$$

$$a_{52} = -\frac{4m^2(1-\cos\theta)}{\sqrt{s}\sin\theta}, \quad \text{(A20)}$$

$$a_{53} = \frac{2m^2[m^2(1+\cos\theta) - s]}{s(1+\cos\theta)}. \quad \text{(A21)}$$

The Saclay amplitudes are given in terms of the helicity amplitudes by

$$\begin{Bmatrix}a_s\\ b_s\\ c_s\\ d_s\\ e_s\end{Bmatrix} = \frac{1}{2\sqrt{2}} \times \begin{bmatrix}\cos\theta & -4\sin\theta & \cos\theta & \cos\theta & -\cos\theta\\ 1 & 0 & 1 & -1 & 1\\ -1 & 0 & 1 & 1 & 1\\ 1 & 0 & -1 & 1 & 1\\ -i\sin\theta & -4i\cos\theta & -i\sin\theta & -i\sin\theta & i\sin\theta\end{bmatrix} \times \begin{Bmatrix}a\\ b\\ c\\ d\\ e\end{Bmatrix}. \quad \text{(A22)}$$

Equations (A8) and (A22) can then be used to obtain the transformation from the Saclay amplitudes to the Fermi invariant functions.

[1] M. Garcon and J. W. Van Orden, Adv. Nucl. Phys. **26**, 293 (2001).
[2] R. A. Gilman and F. Gross, J. Phys. G **28**, R37 (2002).
[3] I. Sick, Prog. Part. Nucl. Phys. **47**, 245 (2001).
[4] S. K. Bogner, R. J. Furnstahl, and R. J. Perry, Phys. Rev. C **75**, 061001(R) (2007).
[5] H. Hergert and R. Roth, Phys. Rev. C **75**, 051001(R) (2007).
[6] F. Gross, J. W. Van Orden, and K. Holinde, Phys. Rev. C **41**, R1909 (1990); **45**, 2094 (1992).
[7] Deuteron Benchmarking Project, see http://hule.fiu.edu/highnp/deubenchmarking.htm

[8] Jefferson Lab Experiment E-94-017, spokespersons W. Brooks and M. Vineyard.
[9] A. Larson, G. A. Miller, and M. Strikman, Phys. Rev. C **74**, 018201 (2006).
[10] W. Cosyn, M. C. Martinez, and J. Ryckebusch, Phys. Rev. C **77**, 034602 (2008); W. Cosyn, M. C. Martinez, J. Ryckebusch, and B. Van Overmeire, *ibid*. **74**, 062201(R) (2006); B. Van Overmeire and J. Ryckebusch, Phys. Lett. **B644**, 304 (2007); J. Ryckebusch, W. Cosyn, B. Van Overmeire, and C. Martinez, Eur. Phys. J. A **31**, 585 (2007).
[11] J. M. Laget, Phys. Rev. C **73**, 044003 (2006); J. M. Laget, arXiv:nucl-th/0507035.
[12] B. Clasie *et al*., Phys. Rev. Lett. **99**, 242502 (2007).
[13] J. Ryckebusch, W. Cosyn, B. Van Overmeire, and C. Martinez, Eur. Phys. J. A **31**, 585 (2007); J. Ryckebusch, P. Lava, M. C. Martinez, J. M. Udias, and J. A. Caballero, Nucl. Phys. **A755**, 511 (2005); P. Lava, M. C. Martinez, J. Ryckebusch, J. A. Caballero, and J. M. Udias, Phys. Lett. **B595**, 177 (2004); L. L. Frankfurt, W. R. Greenberg, G. A. Miller, M. M. Sargsian, and M. I. Strikman, Z. Phys. A **352**, 97 (1995).
[14] Jefferson Lab Experiment E01 - 020, spokespersons W. Boeglin, M. Jones, A. Klein, P. Ulmer, J. Mitchell and E. Voutier.
[15] K. S. Egiyan *et al*. (CLAS Collaboration), Phys. Rev. Lett. **96**, 082501 (2006); K. S. Egiyan *et al*. (CLAS Collaboration), Phys. Rev. C **68**, 014313 (2003).
[16] A. Maschinot, Ph.D. thesis, MIT, 2005; includes BLAST data from MIT Bates.
[17] G. Gilfoyle, spokesperson, Jefferson Lab Hall B, E5 run period; G. P. Gilfoyle (CLAS Collaboration), Bull. Am. Phys. Soc., Fall DNP Meeting, DF.00010 (2006).
[18] W. Boeglin, spokesperson, proposal to Jefferson Lab PAC 33, 2007.
[19] A. Bussiere *et al*., Nucl. Phys. **A365**, 349 (1981).
[20] P. E. Ulmer *et al*., Phys. Rev. Lett. **89**, 062301 (2002).
[21] Werner Boeglin, talk at the 2005 workshop on probing microscopic structure of the lightest nuclei in electron scattering at JLab energies and beyond, Trento, Italy, July 25–30, 2005, http://www.fiu.edu/ sargsian/ect05.
[22] E. Voutier, arXiv:nucl-ex/0501020.
[23] M. M. Sargsian, Int. J. Mod. Phys. E **10**, 405 (2001); M. M. Sargsian, T. V. Abrahamyan, M. I. Strikman, and L. L. Frankfurt, Phys. Rev. C **71**, 044614 (2005); L. L. Frankfurt, M. M. Sargsian, and M. I. Strikman, *ibid*. **56**, 1124 (1997).
[24] J. Ryckebusch, D. Debruyne, P. Lava, S. Janssen, B. Van Overmeire, and T. Van Cauteren, Nucl. Phys. **A728**, 226 (2003); D. Debruyne, J. Ryckebusch, W. Van Nespen, and S. Janssen, Phys. Rev. C **62**, 024611 (2000).
[25] C. Ciofi degli Atti and L. P. Kaptari, Phys. Rev. C **71**, 024005 (2005); C. Ciofi delgi Atti and L. P. Kaptari, arXiv:0705.3951 [nucl-th]; C. Ciofi degli Atti, L. P. Kaptari, and D. Treleani, Phys. Rev. C **63**, 044601 (2001).
[26] J. M. Laget, Phys. Lett. **B609**, 49 (2005).
[27] R. Schiavilla, O. Benhar, A. Kievsky, L. E. Marcucci, and M. Viviani, Phys. Rev. C **72**, 064003 (2005).
[28] B. Van Overmeire and J. Ryckebusch, Phys. Lett. **B650**, 337 (2007).
[29] S. Jeschonnek, Phys. Rev. C **63**, 034609 (2001).
[30] C. Ciofi degli Atti, L. P. Kaptari, and H. Morita, Nucl. Phys. **A782**, 191 (2007).
[31] F. Gross, Phys. Rev. **186**, 1448 (1969); Phys. Rev. D **10**, 223 (1974); Phys. Rev. C **26**, 2203 (1982).
[32] J. W. Van Orden, N. Devine, and F. Gross, Phys. Rev. Lett. **75**, 4369 (1995).
[33] J. Adam, J. W. Van Orden, and F. Gross, Nucl. Phys. **A640**, 391 (1998).
[34] R. A. Arndt, W. J. Briscoe, I. I. Strakovsky, and R. L. Workman, Phys. Rev. C **76**, 025209 (2007); data available through SAID, http://gwdac.phys.gwu.edu/.
[35] A. S. Raskin and T. W. Donnelly, Ann. Phys. (NY) **191**, 78 (1989).
[36] V. Dmitrasinovic and F. Gross, Phys. Rev. C **40**, 2479 (1989).
[37] S. Jeschonnek and T. W. Donnelly, Phys. Rev. C **57**, 2438 (1998); S. Jeschonnek and J. W. Van Orden, *ibid*. **62**, 044613 (2000).
[38] G. Gilfoyle, private communication.
[39] P. Mergell, Ulf-G. Meissner, and D. Drechsel, Nucl. Phys. **A596**, 367 (1996).
[40] H. Arenhovel, W. Leidemann, and E. L. Tomusiak, Phys. Rev. C **46**, 455 (1992); **52**, 1232 (1995); W. Leidemann, E. L. Tomusiak, and H. Arenhovel, *ibid*. **43**, 1022 (1991); F. Ritz, H. Goller, T. Wilbois, and H. Arenhovel, *ibid*. **55**, 2214 (1997).
[41] S. Jeschonnek and T. W. Donnelly, Phys. Rev. C **59**, 2676 (1999).
[42] E. Piasetzky, M. Sargsian, L. Frankfurt, M. Strikman, and J. W. Watson, Phys. Rev. Lett. **97**, 162504 (2006).
[43] A. Bianconi, S. Jeschonnek, N. N. Nikolaev, and B. G. Zakharov, Phys. Lett. **B343**, 13 (1995); Phys. Rev. C **53**, 576 (1996); Nucl. Phys. **A608**, 437 (1996).